Update of the HTSI method: Application to the characterization of mechanical properties of CaF2 from RT to 800°C

Gabrielle Tiphéne, Benedicte Adogou, Gaylord Guillonneau, Guillaume Kermouche, Jean-Michel Bergheau, Warren C. Oliver, Jean-Luc Loubet

Update of the HTSI method : application to the characterization of mechanical properties of CaF_2 from RT to 800 °C

Gabrielle Tiphéne[1,*], Benedicte Adogou[2], Gaylord Guillonneau[3], Guillaume Kermouche[2], Jean-Michel Bergheau[4], Warren C. Oliver[5], and Jean-Luc Loubet[3]

[1]*Institute of Mechanics, Materials and Civil Engineering (iMMC), UCLouvain, B-1348, Louvain-la-Neuve, Belgium*
[3]*Ecole Centrale de Lyon, CNRS, ENTPE, LTDS, UMR5513, 69130 Ecully, France*
[2]*Mines Saint-Etienne, CNRS, UMR5307 LGF, Centre SMS, 42023 Saint Etienne, France*
[4]*Ecole Centrale de Lyon, CNRS, ENTPE, LTDS, UMR5513, ENISE, 42023 Saint Etienne, France*
[5]*KLA Corporation, USA*
[*]*Corresponding author: gabrielle.tiphene@uclouvain.be*

Abstract

The High-Temperature Scanning Indentation (HTSI) method [1] allows for the characterization of material mechanical properties quasi-continuously over a large temperature range in 1-day experiments, based on a cycle with a constant maximum load applied regardless of the temperature. For materials exhibiting an Indentation Size Effect (ISE), the variations in hardness with temperature can stem from both temperature and ISE. It is challenging to differentiate their impact on the mechanical properties. So, a new 1-second indentation cycle was implemented, with an adjustment of the applied maximum load to control the maximum achieved depth across temperatures. It allows for the determination of mechanical properties at a given maximum depth over a wide temperature range.

This methodology has been applied to CaF_2 single-crystal from RT to 800 °C. It enables the characterization of this material at 1000 nm depth over the entire temperature range.. The obtained results are consistent with conventional indentation results.

Keyword nano-indentation; Ca; F; crystal; extreme environment; hardness; in situ; nanoscale

Highlights

- A new 1-second cycle allowing maximum-depth control throughout thermal cycling for the HTSI method has been implemented
- This methodology was applied on CaF_2, known to present a ISE in temperature
- Mechanical and creep properties of CaF_2 were determined from RT to 800 °C

I Introduction

Calcium fluoride is an ionic metal used in various industries for its properties in temperature (lubrification [2–5], optics [6–9], etc.). It has been characterized at high temperature [10] but since it is quite brittle at room temperature [11], characterizing its mechanical properties from room temperature to 800 °C is quite complicated.

Nanoindentation testing allows the characterization of small samples at room temperature [12, 13]. The classical Constant Stiffness Measurement method (CSM) provides properties along the tested depth at a given strain rate [14]. Combining these tests with long-term indentation creep tests [15, 16] as well as relaxation tests [16, 17] now gives access to mechanical properties over 8 orders of magnitude in strain rate.

With the recent development of high-temperature nanoindentation devices [18, 19], nanoindentation testing can be carried out up to 1000 °C. Creep properties can then be determined at various temperatures using the methods implemented for room temperature testing. However, classical CSM, creep, and relaxation indentation tests require precise control of thermal equilibrium during the tests

[17]. Carrying out such tests at high temperatures remains a challenge to overcome, and is still time-consuming.

The High-Temperature Scanning Indentation (HTSI) method [1] allows performing 1-second indentation tests while heating the sample, providing access to mechanical properties over the entire studied temperature range. The idea is that performing 1-second indentation tests during slow heating (a few $^{\circ}\mathrm{C/min}$) greatly reduces the impact of thermal drift. The indentation cycle is programmed in load-control, meaning the same maximum load is applied regardless of the temperature. Moreover, because of the short duration of the indentation cycle, CSM cannot be easily implemented during loading [20–22]. Thus, mechanical properties are only determined at the maximum depth point. As hardness is expected to decrease with temperature, the tested volume increases significantly with temperature. However, to better understand the source of variations observed during testing, it is preferred to test the same volume of material. Moreover, some materials exhibit an Indentation Size Effect (ISE), where their mechanical properties change with depth [23]. Changing both temperature and testing depth does not allow distinguishing the impact of each phenomenon on changes in behavior. So is there a way to perform indentation tests to characterize CaF_2 mechanical properties from RT to $800\,^{\circ}\mathrm{C}$ without impact of the ISE?

In the present work, we propose an updated version of the indentation cycle used in [1] to address some of the previously identified problems. A new strategy is presented, allowing for a change from maximum load-controlled to maximum depth-controlled indentation cycle. Then, this strategy is applied to characterize the mechanical (creep and hardness) properties of CaF_2 single crystals. Finally, discussion on the proposed method and the results is carried out to identify their limitations.

II Updates of the High-Temperature Scanning Indentation Technique

II.1 Preparation of the thermal cycle

As already presented in [1, 24], the HTSI method consists of applying multiple short indentation tests along a specific thermal cycle. To ensure thermal equilibrium throughout the tests, calibration steps are required. First, it is assumed that since the tip is quite small ($1\,\mathrm{mm}$ to $2\,\mathrm{mm}$ long) and usually made of conductive materials [18], the temperature of the contact point is the same as the one measured at the tip backside (see Figure S1). So one should start by defining the thermal cycle to apply to the tip. Then, temperature calibration steps are performed following the method proposed by Minnert et al. [19]. For a given temperature on the tip side, one should determine the temperature to apply at the back of the sample to achieve thermal equilibrium at the contact point. We recommend performing such calibration steps at least at two temperatures in the studied temperature range. From experiments, if the maximum studied temperature is lower than approximately $700\,^{\circ}\mathrm{C}$, the difference between the settings is believed to evolve quasi linearly, as radiation is not expected to play a major role in the heating. Once the settings have been correctly determined, the thermal cycle to be applied on the sample side can be constructed. It should be noted that the heating rate on the tip and sample may be different since the maximum temperatures to be achieved are usually different. The main difficulty here is to have extremely precise control of the temperatures during the experiments. A schematic representation of the preparation of the thermal cycle is presented in Figure S1 in the Supplementary Materials.

II.2 Updates of the indentation cycle

II.2.a From quarter-sinus to half-sinus loading

The indentation cycle proposed by Tiphéne et al. [1] allows performing an indentation test in $0.8\,\mathrm{s}$ but induces a burst effect at the beginning of the loading step on all tested materials. Some may believe that it is a "pop-in" effect [24]. However, in this case, it is believed to be an experimental artifact since it was also observed on fused silica (see Figure S2). It is probably due to the infinite value of the derivative of the load at the starting point of the test. To overcome this effect, the quarter sinus loading function used in [1] has been replaced by a half-sinus loading function.

$$P(t) = P_{max} \sin\left(\frac{\pi t}{2t_{load}}\right) \Rightarrow P(t) = \frac{P_{max}}{2}\left(1 - \cos\left(\frac{\pi t}{t_{load}}\right)\right) \tag{1}$$

With P_{max} the maximum load and t_{load} the loading time. The corresponding loading cycles have been plotted in Figure S2(a). In Figure S2(b), the application on fused silica shows the disappearance of this artifact at the beginning of loading.

II.2.b From maximum load control to maximum depth control

As hardness usually decreases with increasing temperature, the tested volume increases when performing maximum load-controlled HTSI experiments [1]. However, some materials presents an Indentation Size Effect (ISE) at room temperature : the mechanical properties depend on the tested depth. Then, the hardness reduction observed during testing is due to both the temperature and the increased maximum depth. As, the ISE may depend on temperature, it is not possible to predict its changes in temperature and so to correct its effect based on room temperature measurements. To reduce the impact of the ISE and better control the tested volume, a cycle controlled in displacement would be much better. As it is quite complicated to implement a 1-second depth-controlled indentation cycle on the used force-controlled nanoindentation device, a different approach is used. The idea is to adapt the applied maximum load between each test using the result of the previous test. Under the hypothesis that the hardness does not change much between two tests, it is then possible to predict the load to target to always perform tests at a given maximum depth. Such a strategy requires a sample where hardness does not vary in space nor is expected to vary abruptly (due to microstructure changes, for instance [24]) during the thermal cycle. So the maximum load in equation 1 for test i would be calculated using the results of test $i-1$:

$$P_{max}^{i} = P_{max}^{i-1}\left(\frac{h_{target}}{h_{max}^{i-1}}\right)^{2} \tag{2}$$

With h_{target} the maximum depth that one wants to reach at all temperatures, and P_{max}^{i-1} and h_{max}^{i-1} representing the maximum load and depth reached in test $i-1$, respectively.

II.3 Nanoindentation analysis

Analysis of the HTSI results is performed using a Python code. The classical definitions of hardness, Young's modulus, etc., used in nanoindentation, are implemented. To confirm those results, CSM at constant strain rate (CSR), creep, and relaxation tests are also performed at different temperatures. The equations for the analysis are reminded in the following section. HTSI values are determined at the maximum depth point, while the CSM loading gives the mechanical properties all along the depth. Depending on the contact, pile-up or sink-in is observed: one should then prefer Loubet's model [13] or Oliver and Pharr's model [12].

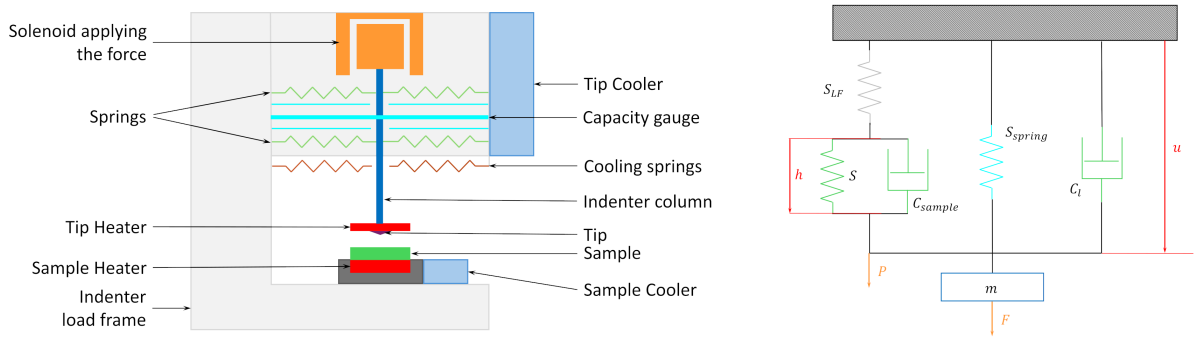

Figure 1: Schematic representation of the indentor and corresponding rheological model. We apply the raw force F and measure the raw displacement u and the raw stiffness K. To determine the mechanical properties, the load P, depth h and contact stiffness S are required. Adapted from [25].

II.3.a Determination of modulus and hardness

We measure the raw force F and the raw displacement u through the solenoid and capacity gauge of Figure 1. The total stiffness K is then:

$$K = \frac{dF}{du} \tag{3}$$

The load is defined as:

$$P = F - S_{spring}u \tag{4}$$

and the depth:

$$h = u - \frac{P}{S_{LF}} = u\left(1 + \frac{S_{spring}}{S_{LF}}\right) - \frac{F}{S_{LF}} \tag{5}$$

The contact stiffness S is related to K though:

$$\frac{1}{S} = \frac{1}{K - S_{spring}} - \frac{1}{S_{LF}} \tag{6}$$

with $S_{S_{LF}}$ denoting the load frame stiffness, calibrated on fused silica. It is supposed to stay constant in temperature [19]. In the following, the spring stiffness term is neglect in regard of its value ($\approx 700\,\mathrm{N/m}$) compared to the total stiffness ($\approx 5 \times 10^5\,\mathrm{N/m}$).

For HTSI tests, the total stiffness K is calculated using the unloading part of the indentation cycle [1], assuming a linear fit.

$$F = K(u - u_0) \tag{7}$$

with u_0 the raw displacement when the force is null.

In the present work, SEM observation confirmed that no pile-up phenomenon was observed on post-mortem indents on CaF_2. Oliver and Pharr's [12] model was then used to determine the contact depth h_c in this case. According to this model:

$$h_c = h - 0.75\frac{P}{S} \tag{8}$$

with h, the measured depth, P the applied load and S the contact stiffness.

The contact area is:

$$A_c = \sum_0^n C_i h_c^{2/2^i} \tag{9}$$

with the C_i been calibrated on fused silica. For a perfect Berkovich tip, $C_0 = 24.5$ and the others C_i are null.

The hardness H is defined as:

$$H = \frac{P}{A_c} \tag{10}$$

Through Sneddon work's [12, 13, 26], the stiffness can be related to the reduced modulus:

$$E_r = \frac{S}{2}\sqrt{\frac{\pi}{A_c}} \tag{11}$$

The indentation modulus M [27–29] is then defined as:

$$\frac{1}{M} = \frac{1}{E_r} - \frac{1 - \nu_i^2}{E_i} \tag{12}$$

with E_i and ν_i the tip Young's modulus and Poisson ratio respectively. ν_i was considered constant in temperature. The tip modulus changes in temperature were implemented, following the formula in [18].

In case of homogeneous isotropic materials, the Young's modulus E is then computed as:

$$E = \frac{M}{(1 - \nu^2)} \tag{13}$$

With ν the Poisson ratio of the sample. We are dealing here with single-crystal samples, whose behaviors are anisotropic. However, we will still consider that equation 13 holds true in the following. For a more precise analysis, the work of [27–30] should be consulted.

II.3.b Creep properties

To characterize the creep properties of the sample, the representative stress σ_r is first computed using the method described in [31]:

$$\sigma_r = \frac{H}{\gamma} = \frac{\xi_3 \cot\theta}{\xi_1 \cot\theta - (1 - \xi_2)\frac{H}{E}} H \tag{14}$$

with θ the equivalent conical angle (70.32° for a Berkovich tip) and ξ_1, ξ_2 and ξ_3 characteristic tip's parameters. For HTSI tests, the hardness is calculated along the creep segment using the unloading contact stiffness to compute the contact depth (see Equation 8).

During the long-term creep tests, the load is maintained constant, and the contact stiffness is measured continuously throughout the holding period. The strain rate is then defined as described in [16]:

$$\dot{\varepsilon}_{creep} = \frac{\dot{S}}{S} \tag{15}$$

In the case of the relaxation tests, the stiffness is held constant [17]. Therefore, the strain rate can no longer be defined through the stiffness variations. Following the analysis of Baral et al. [16], the strain rate is defined using the variations in representative stress:

$$\dot{\varepsilon}_{relaxation} = -\frac{1}{E}\frac{d\sigma_r}{dt} \tag{16}$$

Finally, as the HTSI tests are quite quick, stiffness is not recorded during the test. Therefore, the strain rate is then defined using the classical definition [32, 33]:

$$\dot{\varepsilon}_{HTSI} = \frac{\dot{h}}{h} \tag{17}$$

An example of the calculation of the creep properties in the case of HTSI tests is plotted in Figure S3 in the Supplementary Material.

Supposing that the material follows a Norton-Hoff creep law:

$$\dot{\varepsilon} = \alpha\sigma_r^{1/m}\exp\left(-\frac{Q}{RT}\right) \tag{18}$$

with α a pre-exponential factor, m the strain-rate sensitivity, Q the creep activation energy, R the gas constant and T the absolute temperature. At a given temperature, one can determine the strain rate sensitivity through [15, 16]:

$$m = \frac{d\ln(\sigma_r)}{d\ln(\dot{\varepsilon})} \tag{19}$$

One can then calculate the activation volume of creep v_{ac} using the relation described in [15, 16]:

$$v_{ac} = \frac{\sqrt{3}k_BT}{m\sigma_r} \tag{20}$$

with k_B, Boltzmann's constant.

In nanoindentation, one should exercise caution when comparing creep and relaxation tests [16]. Strain rate sensitivity values obtained here were lower than 0.1, so the representative strain rate definition of [16] was not used.

III Results

III.1 Interest in the maximum depth-controlled indentation cycle

This strategy has been applied to a CaF_2 single crystal. Figure 2 presents the changes in the maximum load and depth achieved during the HTSI tests. As observed, the proposed changes in maximum load between each test allow for good control of the maximum depth at various temperatures. Experimentally, false surface detection leads to a false hardness value near 40 °C. This results in a significant decrease in the applied load. However, the system corrects itself quickly (within 2 to 4 indents), and the target depth value is once again reached. The error remains quite low throughout the entire temperature range (see Figure 2c). CaF_2 is known to exhibit an Indentation Size Effect (ISE) on hardness [23, 34]. As observed in Figure 2, hardness decreases more rapidly when using a maximum load-controlled cycle instead of a maximum depth-controlled cycle due to this effect.

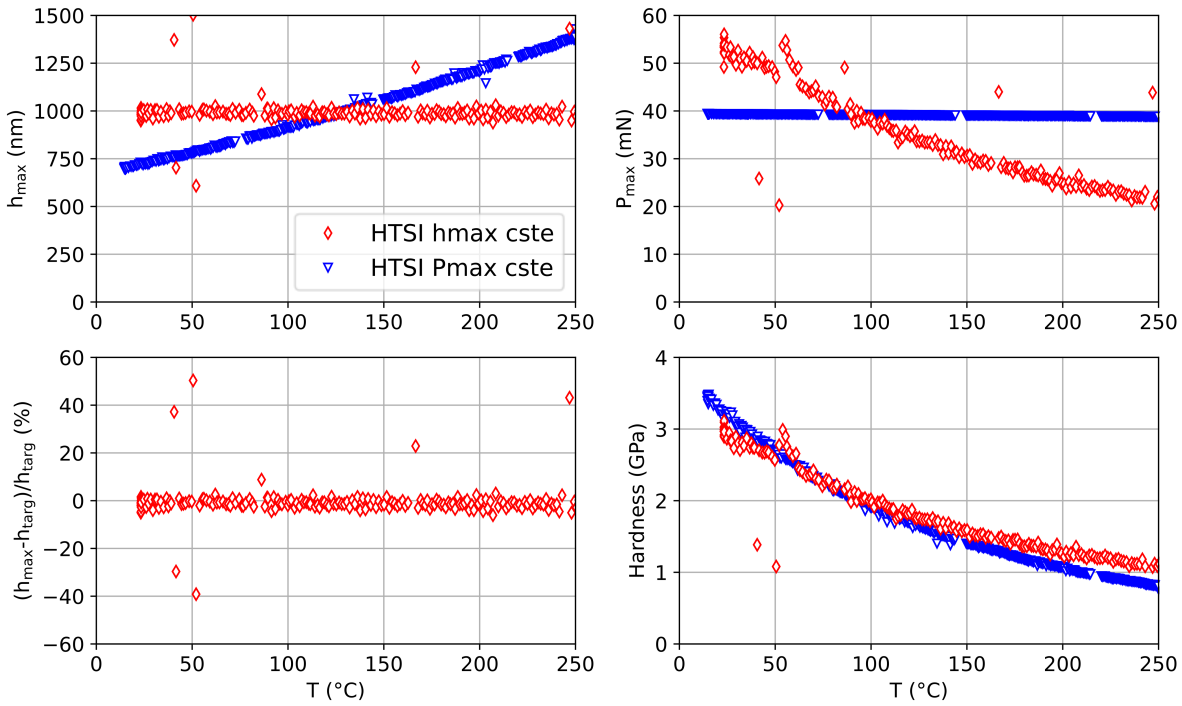

Figure 2: (Top) Maximum depth (left) and load (right) versus temperature measured on CaF_2 during heating. (Purple) Indentation cycle with a target load of $40\,\mathrm{mN}$ at all temperatures. (Cyan) The adapted indentation cycle is used with a $1000\,\mathrm{nm}$ target depth at all temperatures. (Bottom left) Percentage of error on achieved maximum depth compared to target depth for the maximum depth-controlled HTSI tests. Except for the points related to false surface detection, the error stays within $\pm 5\%$. (Bottom right) Corresponding hardness versus temperature curves on CaF_2. The impact of increasing testing depth can clearly be observed on the hardness values here.

III.2 CaF_2 at room temperature

CaF_2 was first characterized at room temperature. Figure 3 presents the hardness and Young's modulus determined by CSM at various loading rates. Mean values at $900\,\mathrm{nm}$ are recap in Table **??**. Values are consistent with literature [23, 34]. As it can be seen, there is no clear impact of the strain rate on the modulus. However, on hardness, there is both an impact of loading rate [35] and a size effect [23]. For future analysis, when comparing results, they are taken at a depth of $1000\,\mathrm{nm}$.

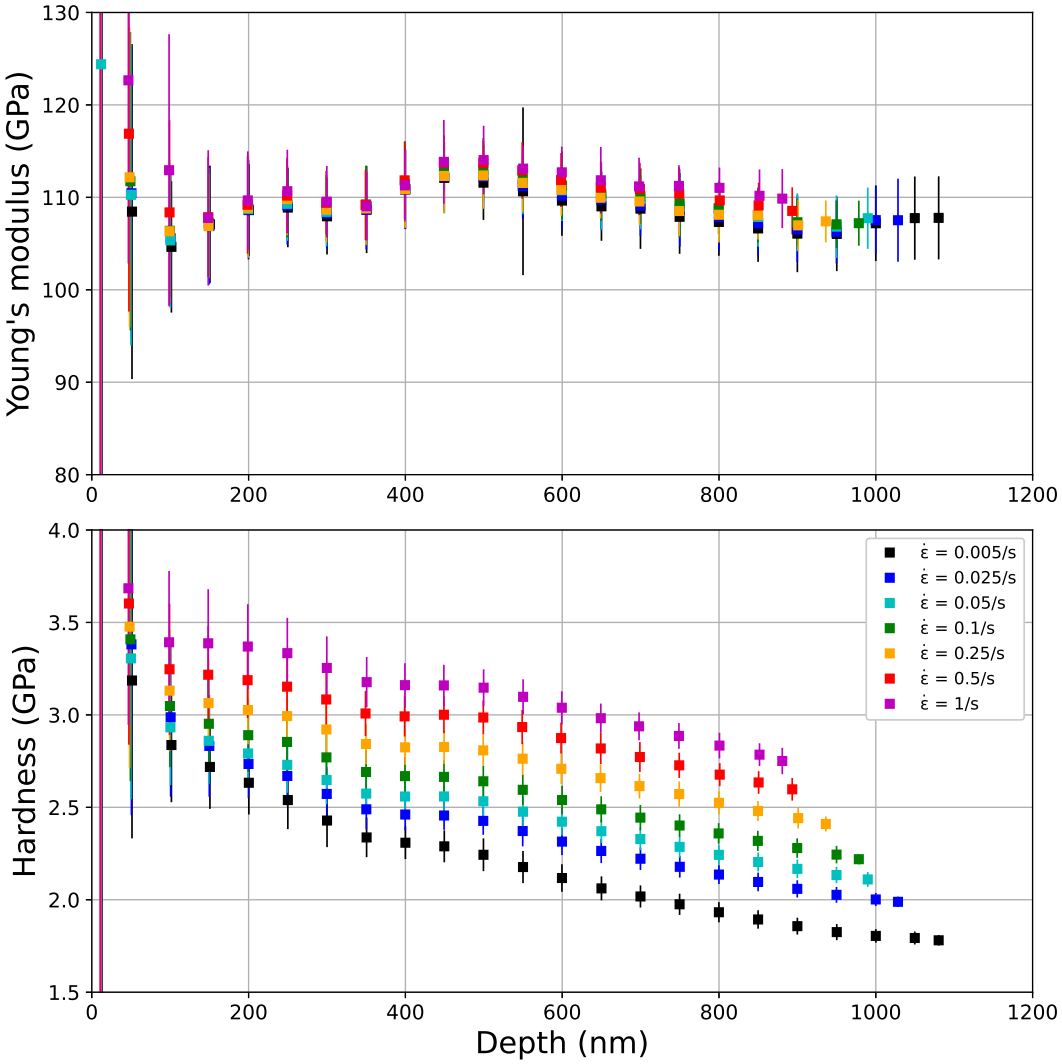

Figure 3: Impact of strain rate on hardness and Young's modulus at RT on CaF_2 samples. The given values are the mean $\pm$ 3std values. 5 to 10 indents were carried out at each strain rate. Contrary to modulus, hardness is sensitive to strain rate and exhibits a size effect. Unfortunately, the tip used to get those results has been damage by HT indentation tests, which explain the oscillations that can be observed at low depths.

To gather more information on the creep behaviors of CaF_2 at room temperature, indentation creep and relaxation tests, as well as constant high-strain rate tests, were conducted. The results of strain rate versus modulus-compensated stress are plotted in Figure 4. The evolution is consistent across the tests. However, the variations are not linear at all, and the sample appears more sensitive to strain rate as it increases. This behavior is unexpected for FCC structures but quite common in BCC structures [36].

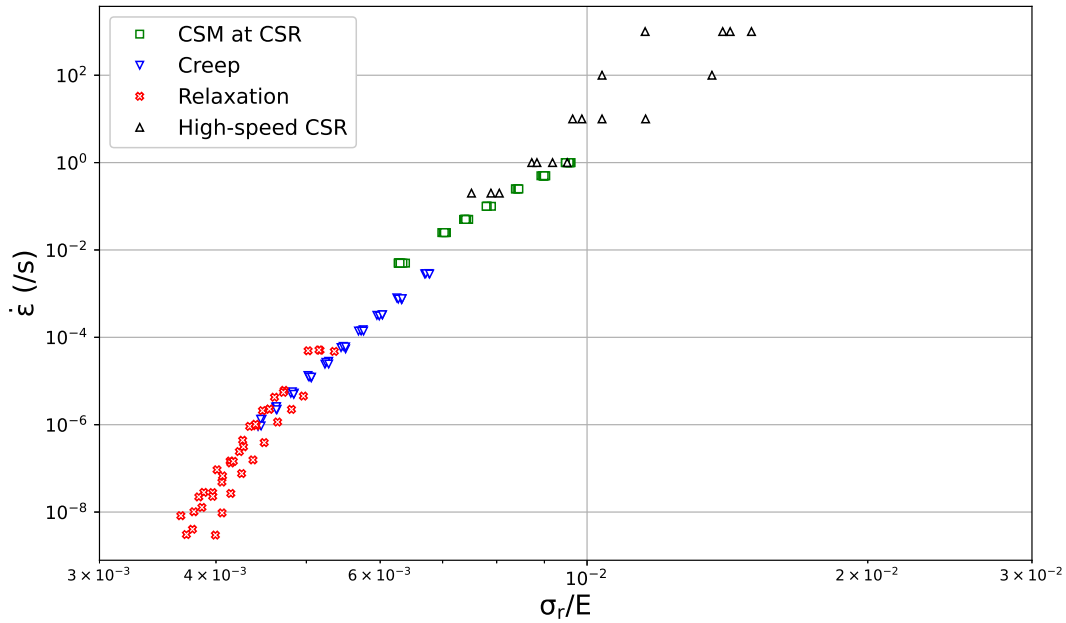

Figure 4: Stress versus strain rate curve on CaF_2 single-crystals at room temperature, obtained using various indentation tests. Non-linearity indicates different creep behaviors, depending on strain rate and temperature.

III.3 CaF_2 at high temperatures

III.3.a Mechanical properties in temperature

Young's modulus and hardness changes with temperature are plotted in Figure 5. The black curve corresponds to the expected changes in Young's modulus for CaF_2 along the studied orientation [35, 37]. As expected, the measured values decrease with temperature. However, the absolute values vary around the expected value at a given temperature. In the HTSI tests at temperatures higher than $750\,^{\circ}\mathrm{C}$, the variations in Young's modulus are quite unreliable. Due to issues with the automatic testing, the tests at these high temperatures were conducted manually, and thermal equilibrium is not expected to be achieved. It can be observed that all CSM tests at $200\,^{\circ}\mathrm{C}$ yield very small values.

As previously observed, the hardness value at room temperature depends on the strain rate. A mean strain rate of $2\,\mathrm{s}^{-1}$ is estimated during loading in the HTSI tests, which is consistent with the higher hardness value obtained at room temperature. When increasing the temperature, hardness starts decreasing rapidly until $200\,^{\circ}\mathrm{C}$. At higher temperatures, it still decreases but less rapidly. A slight drop in hardness is observed around $500\,^{\circ}\mathrm{C}$ before the decrease in hardness smoothens again until $750\,^{\circ}\mathrm{C}$ approximately. Strangely, an increase in hardness is observed near $800\,^{\circ}\mathrm{C}$.

Hardness variations with temperature are consistent with those measured by Deadmore [11], although the absolute values differ. This discrepancy is expected to be due to differences in tested depth since Vickers hardness yields results at larger depths compared to nanoindentation tests. Finally, the impact of strain rate on hardness seems to decrease with increasing temperature.

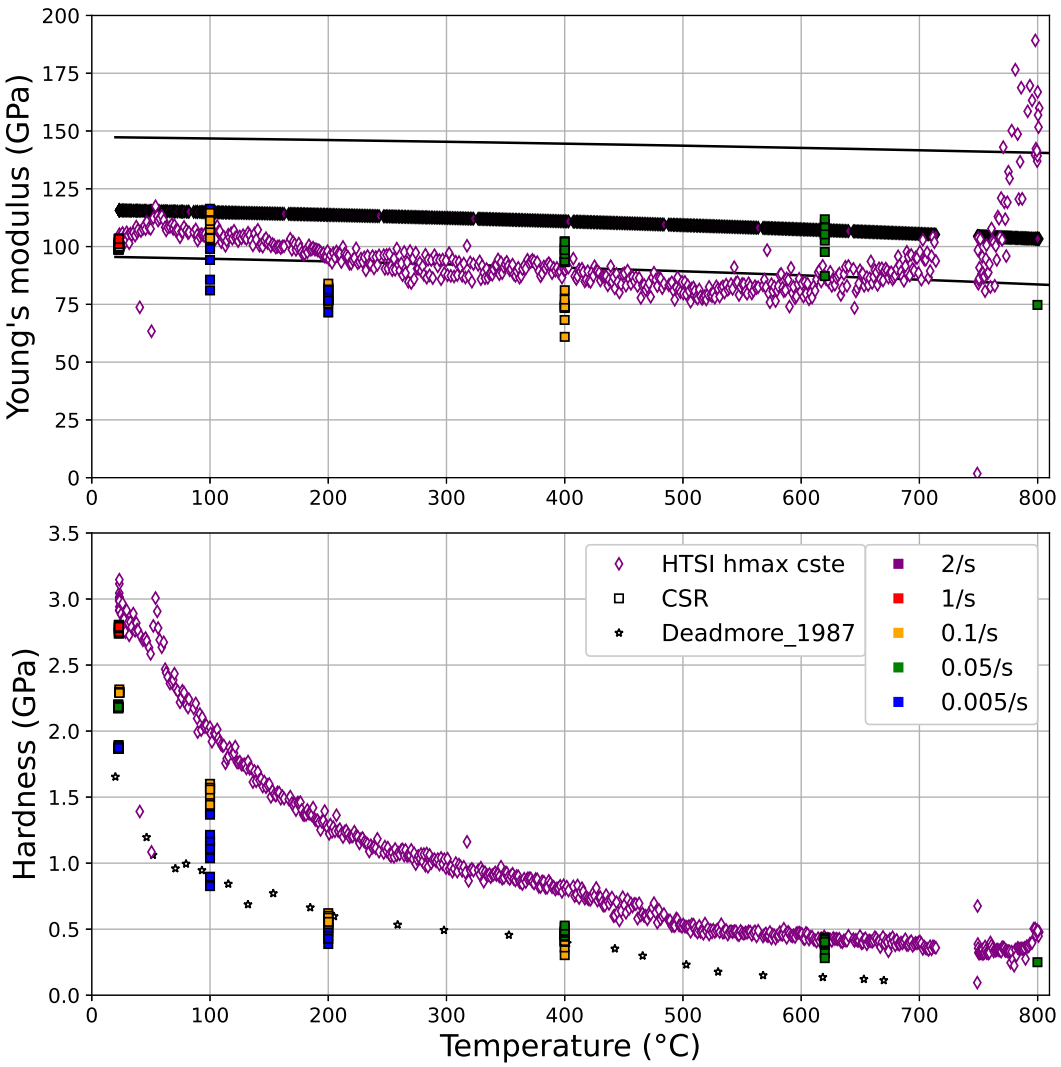

Figure 5: (Top) Young's modulus and (bottom) hardness changes with temperature for CaF_2 single-crystal. All data are measured at a depth of $1000\,\mathrm{nm}$. The colors indicate the strain rate during loading (mean values for HTSI tests). Strain rate greatly impacts the hardness values at room temperature, but its impact decreases at high temperature. The hardness changes are consistent with literature data [11]. On the Young's modulus data, the black lines represent Voigt (top) and Reuss (bottom) bounds. The black diamonds show the expected Young's modulus changes, given the crystal orientation. The HTSI data appears consistent with these values up to $750\,^{\circ}\mathrm{C}$.

III.3.b Creep properties

To obtain the creep properties of CaF_2 at different temperatures, creep and relaxation tests were conducted. The strain rate versus modulus-compensated stress curves at all temperatures can be founded in Figure S4 in the supplementary material. Classical constant strain rate (CSR) and creep indentation tests are compared to relaxation tests and HTSI results.

Under the assumption that a single creep mechanism dominates the creep behavior of CaF_2 (Norton-Hoff creep law, Equation 18), the master curve has been plotted in Figure 6 for an activation energy of $100\,\mathrm{kJ/mol}$. Such analysis give access to more than 20 orders of magnitude for the temperature-compensated strain rate.

The different tests overlap quite well, and the trend at high temperatures appears consistent with the results of Sadrabadi [10]. However, assuming a constant value of the activation energy over this wide temperature range is questionable since, according to the literature, we would expect it to increase with temperature: Oneill *et al.* [38] found an energy of $42\,\mathrm{kJ/mol}$ for temperatures below $300\,^{\circ}\mathrm{C}$, while

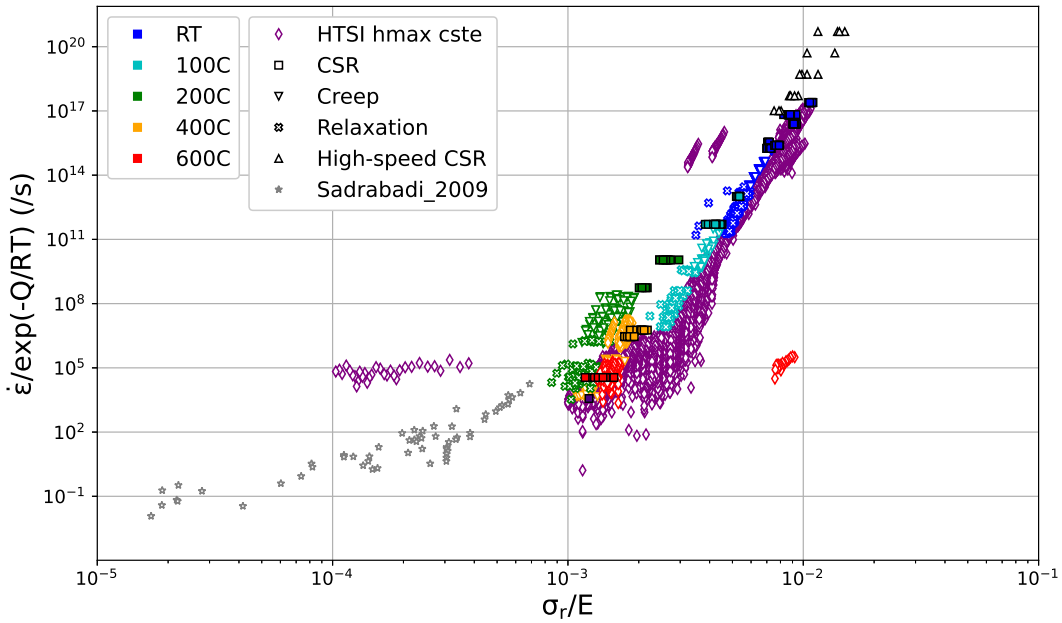

Figure 6: Master curve obtained for CaF_2 with an activation energy of $100\,\mathrm{kJ/mol}$. The various indentation tests exhibit good agreement, and the trend is consistent with the high-temperature tests conducted by Sadrabadi [10].

Mekala [39] proposed an apparent activation energy (in $\mathrm{J/mol}$) for creep following:

$$Q(T) = 8.31(20.8\,T(K) + 7640) \tag{21}$$

when the temperature is in the range $400\,^\circ\mathrm{C}$ to $927\,^\circ\mathrm{C}$ ($180\,\mathrm{kJ/mol}$ to $271\,\mathrm{kJ/mol}$).

The strain rate sensitivity and activation volume have been plotted against the temperature-compensated strain rate in Figure 7. At room temperature, the activation volume is relatively low (ranging from 1 to $5b^3$ depending on the strain rate). An increase in temperature or a decrease in strain rate leads to an increase in this volume.

The activation volume appears to increase linearly up to $200\,^\circ\mathrm{C}$. Interestingly, the activation volume from the HTSI tests increases more rapidly than that from the creep and relaxation tests between $200\,^\circ\mathrm{C}$ and $400\,^\circ\mathrm{C}$. However, at higher temperatures, the HTSI results align once again with those of the creep and relaxation tests. At high temperatures, the trend is consistent with the results of Sadrabadi [10].

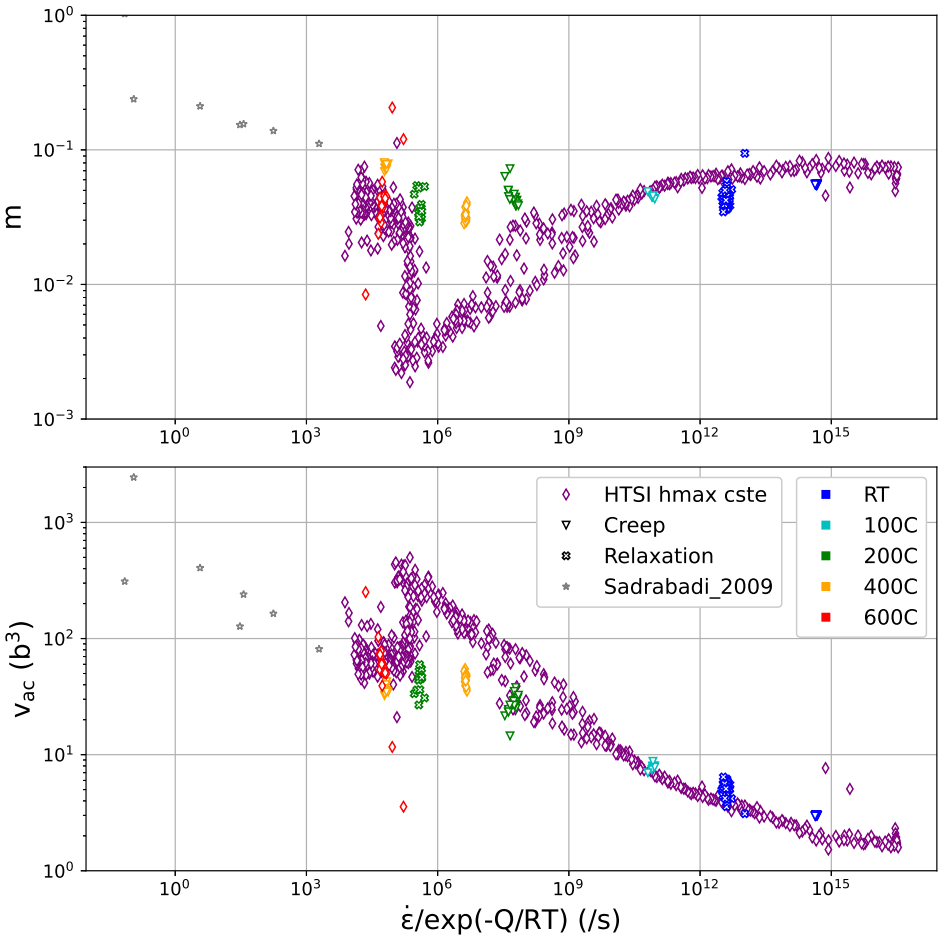

Figure 7: (Top) Strain rate sensitivity and (bottom) activation volume for creep versus temperature-compensated strain rate ($Q = 100\,\mathrm{kJ/mol}$). The results show consistency at both low and high temperatures (for $x > 1 \times 10^{10}$ or $x < 1 \times 10^{6}$). However, in the intermediate range, there appear to be two distinct behaviors, corresponding to the HTSI tests conducted between $200\,^{\circ}\mathrm{C}$ and $500\,^{\circ}\mathrm{C}$.

IV Discussion

IV.1 On the HTSI method

IV.1.a Impact of temperature control on H and E

As observed previously (Figure 5), changes in hardness and Young's modulus with temperature appear consistent, at least up to $750\,^{\circ}\mathrm{C}$ for the modulus. In Figure 8, we plot the maximum depth, load, stiffness, contact depth and area, reduced modulus, Young's modulus, and hardness versus temperature determined by HTSI. It is worth mentioning that the control of the achieved maximum depth is satisfactory across the studied temperature range. Although there is some scattering, it results in a constant contact depth and contact area. Consequently, variations in hardness are primarily attributed to fluctuations in maximum load. Conversely, changes in reduced modulus (and consequently Young's modulus) are primarily influenced by variations in stiffness.

A detailed analysis of the measurements errors impact on the properties can be founded in the supplementary materials (Section S.III.). Considering Figure S5, it is evident that the error in stiffness will significantly impact Young's modulus but will have less impact on the contact depth, contact area, and hardness. For this reason, the authors have more confidence in the hardness data and attribute its variations to the material rather than the measurements. However, they caution that Young's modulus data should be analyzed with care. While the overall trend is usually consistent, the values should be interpreted cautiously.

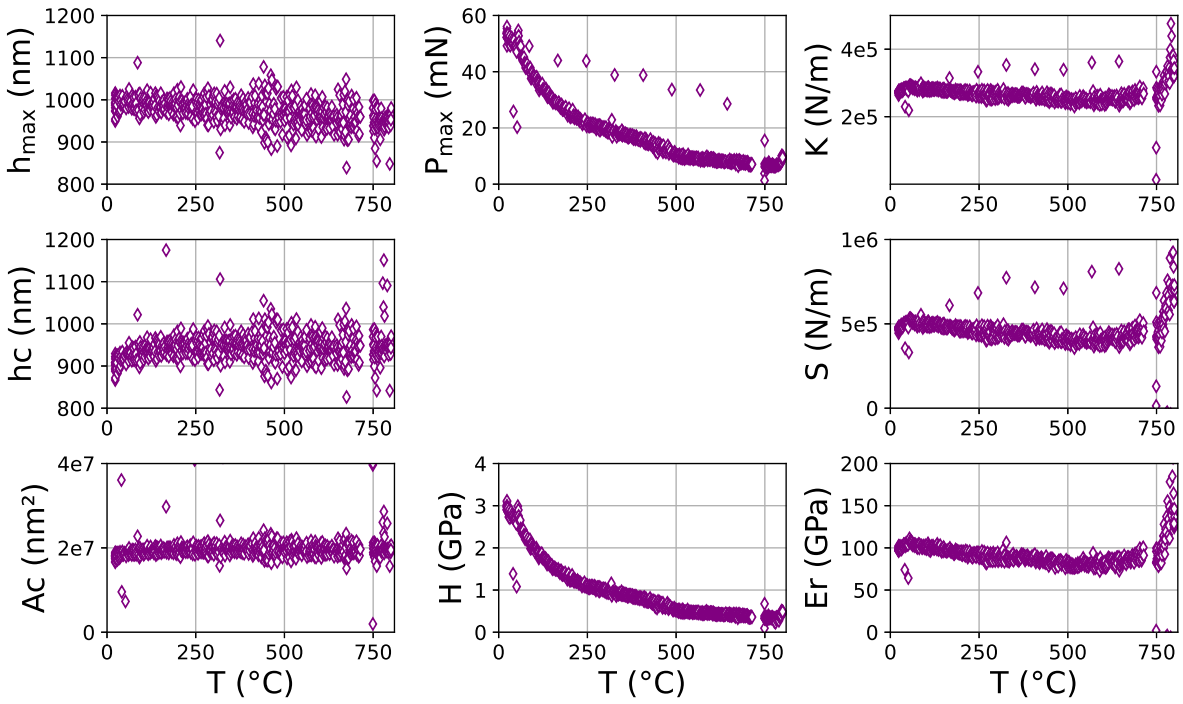

Figure 8: The evolution of maximum depth, load, contact stiffness, contact depth, reduced modulus, contact area, hardness, and Young's modulus with temperature for CaF_2 single-crystal, as determined through HTSI testing, is presented. It is evident that variations in hardness directly correspond to changes in load, while alterations in Young's modulus are associated with fluctuations in contact stiffness.

IV.1.b Control of the achieved maximum depth

As demonstrated previously, the maximum depth control methodology performs well on CaF_2 single-crystal samples. This approach was then applied to annealed copper samples with a grain size of around $50\,\mu m$.

A series of 100 indents was conducted, with the first indent performed at a controlled maximum load. Subsequent ninety-nine indents were conducted with a target maximum depth of either $200\,nm$ or $1000\,nm$ (see Figure 9). As observed, when targeting a maximum depth of $1000\,nm$, the proposed modification leads to an achieved depth in the range of $\pm 20\%$ of this value. This is not that good. Moreover, if the targeted depth is decreased, higher errors are obtained. This technique results in significant discrepancies between the achieved maximum depth and the target depth on annealed copper. These errors are expected to arise from local variations in hardness related to the microstructure of the polycrystalline copper samples. An alternative methodology should be considered to conduct maximum depth control indentation tests on copper (and similar) samples. The assumption of low hardness variations in space is crucial for the successful implementation of this strategy. It should be notice that 20% difference in the maximum achieved depth at all temperatures may be better than multiplying the achieved depth by 2 or 3 between RT and high temperature.

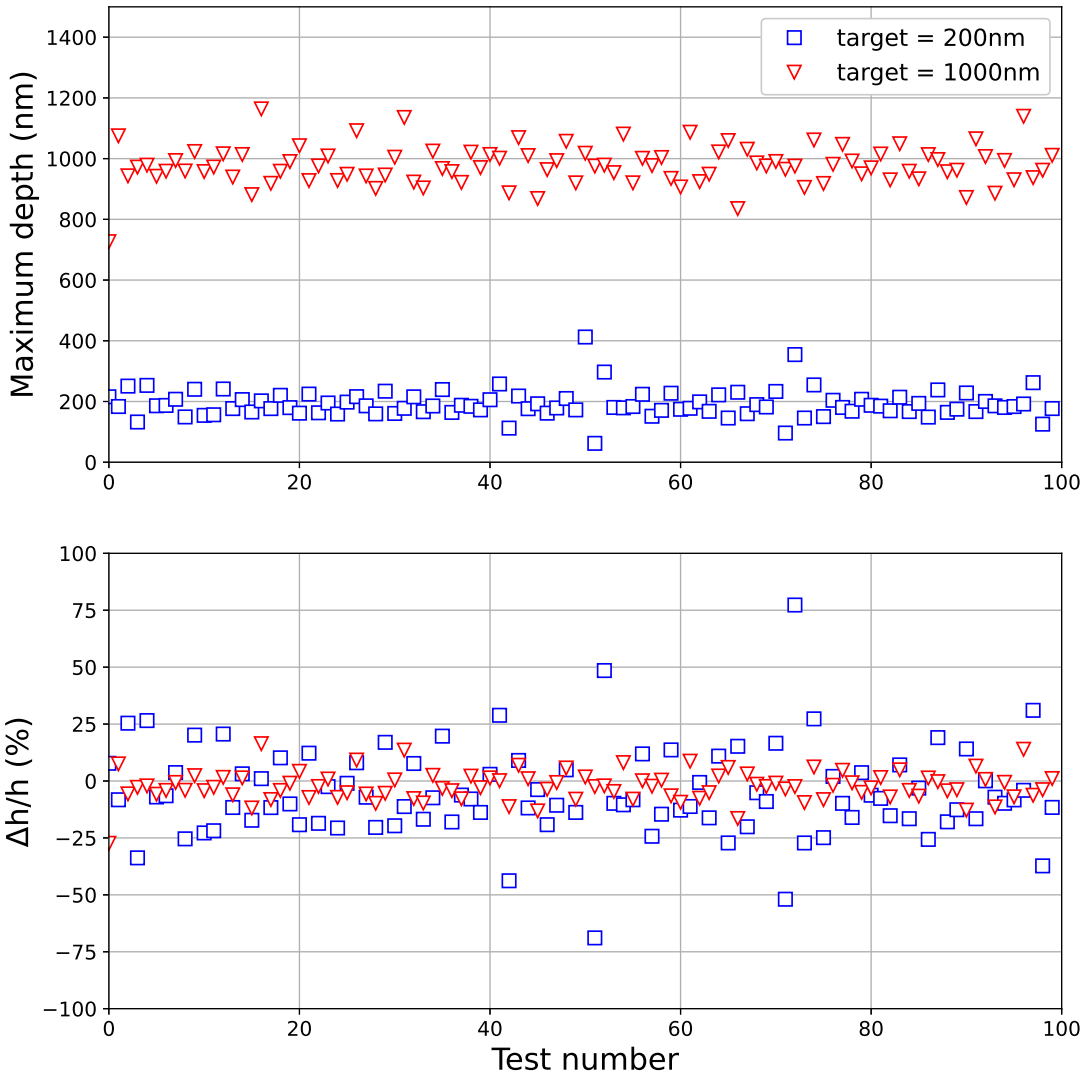

Figure 9: Updated indentation cycle applied to pure annealed copper. (Top) Maximum depth achieved in the test depending on the target depth. Blue squares represent a target depth of 200 nm, while red triangles represent a target depth of 1000 nm. (Bottom) Percentage of error in the achieved depth compared to the target depth.

IV.1.c Creep analysis

As it can be seen in Figure S3, depth increases during the creep segment during the HTSI tests. The same effect can be observed when performing classical creep test. As there is some ISE on the samples, it is expected that part of the hardness decrease comes from this effect. This is an error source in the estimation of the creep properties. However, in the case of HTSI tests, the authors have not yet found a way to correct it since stiffness is not recorded during the creep segment. Moreover, this effect may be negligible compared to the others hypotheses supporting the analysis.

For the classical creep tests is also around 100 nm at RT. As stiffness is measured during the creep segment, it should be possible to correct this effect by estimating the hardness decreases due to ISE before calculating the creep properties. However, the thermal drift may be a larger source of error so we do not correct this effect on the tests.

Finally, the ISE is temperature-dependent effect and is expected to be less and less pronounced as temperature increases. From CSM tests performed at various temperatures, the authors estimated that near 200 °C the hardness variation between 1000 and 1200 nm is 0.025 GPa ($H(200°C) \approx 0.35$ GPa) while the decrease is estimated at 0.1 GPa at RT.

One should be careful when analyzing creep tests following the presented analysis as it may lead to inaccurate results if stationary creep is not reached in the timespan of the creep stage.

IV.2 CaF_2 behaviors

IV.2.a A BCC-like behaviors at RT

At room temperature (RT), the activation volume appears to be quite low (see Figure 7). This observation is intriguing because it suggests that a thermally activated mechanism such as climb could be the controlling mechanism at RT [40]. However, this proposition seems unexpected because climb mechanisms typically require thermal activation, as noted in previous studies [41].

Further insights from studies by Keig et al. [42] and Evans et al. [43] shed light on this phenomenon. These studies suggest that edge dislocations exhibit significantly lower speeds compared to screw dislocations at RT. Additionally, at low temperatures (below 700 °C), vacancies may arise due to the movement of interstitial fluorine ions, resulting in local charges [44]. Evans et al. [43] propose that near RT, a probable controlling mechanism could involve the interaction of edge dislocations with these local charges. In this scenario, edge dislocations would need to overcome electronic barriers to move within the crystal structure.

This behavior bears resemblance to the phenomenon of screw dislocations overcoming Peierls stress in body-centered cubic (BCC) structures at low temperatures [8, 41]. Futher analysis would be required to better understand this behavior.

IV.2.b Changes of behaviors with high temperature

As observed previously, hardness exhibits significant scattering at low temperatures due to strain rate effects. This phenomenon can be attributed to the activation of a low number of gliding systems at low temperatures [38, 45, 46]. Such behavior resembles the characteristics of body-centered cubic (BCC) structures. As the temperature increases, more gliding systems become activated. Near temperatures of around 200 °C [38] and between 400-500 °C [46, 47], an increase in the number of active gliding systems is observed. This trend is consistent with the observed drop in hardness near 500 °C in Figure 5. Finally, at temperatures higher than 600 °C, plasticity is expected to become more isotropic [47].

As observed in Figure 5, an unexpected increase in hardness is observed near 800 °C. This could be attributed to a reaction of the sample with oxygen, resulting in material hardening [11]. After the high-temperature testing, the samples were no longer transparent, indicating a reaction had occurred. SEM observation of the samples (see Figure S6 and S7) revealed the presence of a structure on the sample surface that was not observed before high-temperature testing. EDX analysis (see Figure S8) of this structure showed a depletion of fluorine, replaced by oxygen. This suggests that the sample reacted with oxygen at high temperatures to form calcium oxide [48–50]. It appears that the vacuum level of 1×10^{-2} Pa was insufficient to prevent this reaction.

V Conclusions

This paper presents an update version of the High-Temperature Scanning Indentation technique [1]. It allows determining the mechanical properties of a material at a given depth on the whole studied temperature range. The main points of the article are as follows:

- The 1-second indentation cycle presented in [1] has been modified. HTSI tests are then carried out at a controlled maximum depth all along the thermal cycle. To do so, the applied maximum load is adjusted between each indent, using previous results.

- The old and update cycles have been applied to study the mechanical properties of CaF_2 single-crystals from room temperature up to 200 °C. CaF_2 is known to present a important ISE effect against depth. Thanks to the update methodology, the temperature effect has been separated for the ISE effect and has been clearly quantified here. The error on the maximum achieved depth stays within $\pm 5\%$ on the whole temperature range on CaF_2 single-crystals.

- Error analysis on the determination of hardness and Young's modulus shows that hardness values obtained by HTSI are quite reliable in temperature. On the other hand, stiffness and Young's modulus are greatly impacted by temperature mismatch: one should analyze them with caution.

- Hardness and creep properties of CaF_2 have been characterized from RT to 800 °C. The results are consistent with literature data.

- An equivalence between time and temperature was successfully plotted with an activation energy of $100\,\mathrm{kJ/mol}$. Various indentations tests give consistent results with literature data. A focus on the activation energy values would be required to better understand the mechanism(s) controlling creep depending on temperature and strain rate for this material.

- Hardening of the sample near $800\,^{\circ}\mathrm{C}$ has been related to the reaction of the sample with H_2O or O_2 present in the chambers through EDX characterization.

However, the proposed methodology is based on the assumption of low hardness variations in space. The error on the achieved maximum depth is quite high when applying the technique on annealed copper. It was expected but it means another methodology should be applied for this type of samples. Moreover, having the properties changes again depth at all temperature would be quite interesting. Finding a way to implement a CSM mode at high speed would be a way to go further on this topic.

VI Materials and methods

VI.1 Material

The CaF_2 single crystals were provided by Edmund Optics. These transparent crystals were uncoated flat samples of $2\,\mathrm{mm}$-thickness and $12.5\,\mathrm{mm}$-diameter. Parallelism is lower than 1 arcmin. The physical properties were taken from the literature: Burger's vector [51], lattice parameter [52], elastic constants [53], and Poisson ratio (0.26) [35].

The results on copper samples were obtained using the annealed samples previously used in [24].

VI.2 Experimental set-up

VI.2.a Microstructure characterization

All SEM characterizations were carried out using a Tescan SEM MIRA 3 equipped with an EDX Oxford Instruments XMax $80\,\mathrm{mm}^2$ detector and a EBSD Oxford Instruments NordLys camera. EBSD characterization was carried out to verify the orientation of the CaF_2 single-crystal. EDX analysis was conducted on CaF_2 samples after high-temperature nanoindentation to verify the surface composition. Post-processing was performed using the MTEX MATLAB ToolBox [54].

VI.2.b Nanoindentation testing of CaF_2

Load-controlled nanoindentation tests were conducted using the InSEM HT nanoindentation device (KLA Corporation), which was located inside a vacuum chamber (KLA, TN, USA) or inside a TESCAN SEM (LTDS, France) with a pressure of $1 \times 10^{-2}\,\mathrm{Pa}$. A diamond Berkovich tip was used at room temperature, a sapphire tip was used up to $400\,^{\circ}\mathrm{C}$, and a WC tip was used up to $800\,^{\circ}\mathrm{C}$. Tip calibration was performed on a fused silica sample at ambient conditions prior to any experiments [13, 14]. Between high-temperature tests, the tip was regularly calibrated on fused silica. The specimens were mounted as indicated by Minnert et al. [19]. The minimal distance between each indent was 10 times the contact depth [55]. Temperature settings and controls were conducted in the same way as in [1, 24].

Table 1 presents the various indentation tests that were carried out on the CaF_2 samples. Classical CSM [12, 13] tests, as well as creep [15, 56] and relaxation [17] indentation tests, were conducted between room temperature (RT) and $800\,^{\circ}\mathrm{C}$ after reaching thermal equilibrium. Due to difficulties in maintaining thermal equilibrium for long periods at high temperatures, relaxation tests were only conducted up to $200\,^{\circ}\mathrm{C}$ and creep tests up to $400\,^{\circ}\mathrm{C}$.

HTSI [1] tests were then carried out to obtain the mechanical properties throughout the studied temperature range. The updated version of the indentation cycle was used to control the maximum achieved depth throughout this range. The loading is performed in $0.5\,\mathrm{s}$ which gives a mean strain rate during loading of $2\,\mathrm{s}^{-1}$.

To complete these results, high-speed constant strain rate (HS-CSR) indentation tests at RT were performed on an Alemnis device (depth-controlled device) [57].

Acknowledgments

ChatGPT 3.5 was used to correct the grammar and spelling of the present article.

Table 1: Indentation tests carried out on the CaF_2 samples.

type of test	Temperature	h_{max}	$\dot{\varepsilon}_{loading}$	$t_{holding}$
CSM at constant strain rate (CSR)	RT	$900 \rightarrow 1000\,\mathrm{nm}$	$1 \rightarrow 5 \times 10^{-3}\,\mathrm{s}^{-1}$	-
	$100\,^{\circ}\mathrm{C}$	$1000\,\mathrm{nm}$	$0.1 \rightarrow 5 \times 10^{-3}\,\mathrm{s}^{-1}$	-
	$200\,^{\circ}\mathrm{C}$	$1000\,\mathrm{nm}$	$0.1 \rightarrow 5 \times 10^{-3}\,\mathrm{s}^{-1}$	-
	$400\,^{\circ}\mathrm{C}$	$1000\,\mathrm{nm}$	$0.1 \rightarrow 5 \times 10^{-2}\,\mathrm{s}^{-1}$	-
	$600\,^{\circ}\mathrm{C}$	$1000\,\mathrm{nm}$	$5 \times 10^{-2}\,\mathrm{s}^{-1}$	-
	$800\,^{\circ}\mathrm{C}$	$1000\,\mathrm{nm}$	$5 \times 10^{-2}\,\mathrm{s}^{-1}$	-
Creep	RT	$1000\,\mathrm{nm}$	$0.1\,\mathrm{s}^{-1}$	$10\,\mathrm{h}$
	$100\,^{\circ}\mathrm{C}$	$1000\,\mathrm{nm}$	$0.1\,\mathrm{s}^{-1}$	$1000\,\mathrm{s}$
	$200\,^{\circ}\mathrm{C}$	$1000\,\mathrm{nm}$	$0.1\,\mathrm{s}^{-1}$	$1000\,\mathrm{s}$
	$400\,^{\circ}\mathrm{C}$	$1000\,\mathrm{nm}$	$0.1\,\mathrm{s}^{-1}$	$1000\,\mathrm{s}$
Relaxation	RT	$1000\,\mathrm{nm}$	$0.1\,\mathrm{s}^{-1}$	$10\,\mathrm{h}$
	$100\,^{\circ}\mathrm{C}$	$1000\,\mathrm{nm}$	$0.1\,\mathrm{s}^{-1}$	$1000\,\mathrm{s}$
	$200\,^{\circ}\mathrm{C}$	$1000\,\mathrm{nm}$	$0.1\,\mathrm{s}^{-1}$	$1000\,\mathrm{s}$
ine Half-Sinus Loading	$400\,^{\circ}\mathrm{C}$	$1000\,\mathrm{nm}$	$2\,\mathrm{s}^{-1}$ (mean)	$1\,\mathrm{s}$
	$600\,^{\circ}\mathrm{C}$	$1000\,\mathrm{nm}$	$2\,\mathrm{s}^{-1}$ (mean)	$1\,\mathrm{s}$
HTSI	RT$\rightarrow 800\,^{\circ}\mathrm{C}$ $1.5\,^{\circ}\mathrm{C}/\mathrm{min}$	$1000\,\mathrm{nm}$	$2\,\mathrm{s}^{-1}$ (mean)	$1\,\mathrm{s}$
HTSI	RT$\rightarrow 250\,^{\circ}\mathrm{C}$ $2\,^{\circ}\mathrm{C}/\mathrm{min}$	$750 \rightarrow 1400\,\mathrm{nm}$ $P_{max} = 40\,\mathrm{mN}$	$2\,\mathrm{s}^{-1}$ (mean)	$1\,\mathrm{s}$
HS-CSR	RT	$1000\,\mathrm{nm}$	$1 \rightarrow 1000\,\mathrm{s}^{-1}$	-

Funding

The authors acknowledge support from the CPER MANUTECH which financed the experimental system. This research was funded, in whole or in part, by French National Research Agency, Grant ANR-20-CE08-0022. A CC-BY public copyright license has been applied by the authors to the present document and will be applied to all subsequent versions up to the Author Accepted Manuscript arising from this submission, in accordance with the grant's open access conditions.

Conflict of interest

The authors declare that they have no conflict of interest.

Data Availability

The raw/processed data required to reproduce these findings cannot be shared at this time due to legal reasons.

Code availability

Not applicable

Authors' contributions

Gabrielle Tiphéne: Methodology, Formal Analysis, Investigation, Data curation, Writing - Original draft preparation. **Benedicte Adogou**: Investigation, Writing - Review and Editing corrections **Gaylord Guillonneau**: Writing - Review and Editing corrections, Supervision. **Guillaume Kermouche**: Theoretical frame-work, Writing - Review and Editing corrections. **Jean-Michel Bergheau**: Writing - Review and Editing corrections, Supervision. **Warren C. Oliver**: Conceptualization of this study, Methodology, Software, Resources, Writing - Review and Editing corrections, Supervision. **Jean-Luc Loubet**: Conceptualization of this study, Resources, Writing - Review and Editing corrections, Supervision

References

[1] G. Tiphéne *et al.*, "High-Temperature Scanning Indentation: A new method to investigate in situ metallurgical evolution along temperature ramps," *Journal of Materials Research*, vol. 36, no. 12, pp. 2383–2396, 2021. DOI: 10.1557/s43578-021-00107-7.

[2] H. E. Sliney, T. N. Strom, and G. P. Allen, "Fluoride Solid Lubricants for Extreme Temperatures and Corrosive Environments," *A S L E Transactions*, vol. 8, no. 4, pp. 307–322, 1965. DOI: 10.1080/05698196508972103.

[3] G. H. Liu, F. Robbevalloire, R. Gras, and J. Blouet, "Improvement in tribological properties of chromium oxide coating at high temperature by solid lubricants," *Wear*, vol. 160, no. 1, pp. 181–189, 1993. DOI: 10.1016/0043-1648(93)90419-M.

[4] C. DellaCorte, "The effect of counterface on the tribological performance of a high temperature solid lubricant composite from 25 to 650°C," *Surface and Coatings Technology*, vol. 86–87, pp. 486–492, 1996. DOI: 10.1016/S0257-8972(96)02959-3.

[5] J. H. Ouyang, S. Sasaki, and K. Umeda, "Low-pressure plasma-sprayed ZrO_2–CaF_2 composite coating for high temperature tribological applications," *Surface and Coatings Technology*, vol. 137, no. 1, pp. 21–30, 2001. DOI: 10.1016/S0257-8972(00)00918-X.

[6] A. Bensalah, M. Mortier, G. Patriarche, P. Gredin, and D. Vivien, "Synthesis and optical characterizations of undoped and rare-earth-doped CaF_2 nanoparticles," *Journal of Solid State Chemistry*, Von Schnering 75th Birthday, vol. 179, no. 8, pp. 2636–2644, 2006. DOI: 10.1016/j.jssc.2006.05.011.

[7] J. L. Doualan, P. Camy, R. Moncorgé, E. Daran, M. Couchaud, and B. Ferrand, "Latest developments of bulk crystals and thin films of rare-earth doped CaF_2 for laser applications," *Journal of Fluorine Chemistry*, Advances in Inorganic Fluorine Chemistry, vol. 128, no. 4, pp. 459–464, 2007. DOI: 10.1016/j.jfluchem.2006.12.017.

[8] N. Miyazaki, H. Ogino, Y. Kitamura, T. Mabuchi, and T. Nawata, "Birefringence simulations of annealed ingot of calcium fluoride single crystal by considering creep behavior of ingot during annealing process," in *2009 4th International Microsystems, Packaging, Assembly and Circuits Technology Conference*, Taipei, Taiwan: IEEE, 2009, pp. 2–5. DOI: 10.1109/IMPACT.2009.5382295.

[9] X. Zhong, B. Fan, and F. Wu, "High precision processing CaF2 application research based on the magnetorheological finishing technology," in *Optifab 2017*, vol. 10448, SPIE, 2017, pp. 416–422. DOI: 10.1117/12.2279477.

[10] P. Sadrabadi, P. Eisenlohr, G. Wehrhan, J. Stäblein, L. Parthier, and W. Blum, "Evolution of dislocation structure and deformation resistance in creep exemplified on single crystals of CaF_2," *Materials Science and Engineering: A*, vol. 510–511, pp. 46–50, 2009. DOI: 10.1016/j.msea.2008.04.086.

[11] D. L. Deadmore, "Hardness of CaF_2 and BaF_2 Solid Lubricants at 25 to 670 °C," *NASA Technical Memorandum*, 1987.

[12] W. Oliver and G. Pharr, "An improved technique for determining hardness and elastic modulus using load and displacement sensing indentation experiments," *Journal of Materials Research*, vol. 7, no. 6, pp. 1564–1583, 1992. DOI: 10.1557/JMR.1992.1564.

[13] J. L. Loubet, M. Bauer, A. Tonck, S. Bec, and B. Gauthier-Manuel, "Nanoindentation with a Surface Force Apparatus," in *Mechanical Properties and Deformation Behavior of Materials Having Ultra-Fine Microstructures*, M. Nastasi, D. M. Parkin, and H. Gleiter, Eds., Dordrecht: Springer Netherlands, 1993, pp. 429–447. DOI: 10.1007/978-94-011-1765-4_28.

[14] W. C. Oliver and G. M. Pharr, "Measurement of hardness and elastic modulus by instrumented indentation: Advances in understanding and refinements to methodology," *Journal of Materials Research*, vol. 19, no. 1, pp. 3–20, 2004. DOI: 10.1557/jmr.2004.19.1.3.

[15] V. Maier, B. Merle, M. Göken, and K. Durst, "An improved long-term nanoindentation creep testing approach for studying the local deformation processes in nanocrystalline metals at room and elevated temperatures," *Journal of Materials Research*, vol. 28, no. 9, pp. 1177–1188, 2013. DOI: 10.1557/jmr.2013.39.

[16] P. Baral *et al.*, "Indentation creep vs. indentation relaxation: A matter of strain rate definition?" *Materials Science and Engineering: A*, vol. 781, p. 139 246, 2020. DOI: 10.1016/j.msea.2020.139246.

[17] P. Baral, G. Guillonneau, G. Kermouche, J.-M. Bergheau, and J.-L. Loubet, "A new long-term indentation relaxation method to measure creep properties at the micro-scale with application to fused silica and PMMA," *Mechanics of Materials*, vol. 137, p. 103 095, 2019. DOI: 10.1016/j.mechmat.2019.103095.

[18] J. M. Wheeler and J. Michler, "Indenter materials for high temperature nanoindentation," *Review of Scientific Instruments*, vol. 84, no. 10, p. 101 301, 2013. DOI: 10.1063/1.4824710.

[19] C. Minnert, W. C. Oliver, and K. Durst, "New ultra-high temperature nanoindentation system for operating at up to 1100 °C," *Materials & Design*, vol. 192, p. 108 727, 2020. DOI: 10.1016/j.matdes.2020.108727.

[20] B. Merle, V. Maier-Kiener, and G. M. Pharr, "Influence of modulus-to-hardness ratio and harmonic parameters on continuous stiffness measurement during nanoindentation," *Acta Materialia*, vol. 134, pp. 167–176, 2017. DOI: 10.1016/j.actamat.2017.05.036.

[21] B. Merle, W. H. Higgins, and G. M. Pharr, "Critical issues in conducting constant strain rate nanoindentation tests at higher strain rates," *Journal of Materials Research*, vol. 34, no. 20, pp. 3495–3503, 2019. DOI: 10.1557/jmr.2019.292.

[22] B. Merle, W. H. Higgins, and G. M. Pharr, "Extending the range of constant strain rate nanoindentation testing," *Journal of Materials Research*, vol. 35, no. 4, pp. 343–352, 2020. DOI: 10.1557/jmr.2019.408.

[23] J. Chua *et al.*, "High-temperature nanoindentation size effect in fluorite material," *International Journal of Mechanical Sciences*, vol. 159, pp. 459–466, 2019. DOI: 10.1016/j.ijmecsci.2019.06.020.

[24] G. Tiphéne *et al.*, "Quantification of softening kinetics in cold-rolled pure aluminum and copper using High-Temperature Scanning Indentation," *Materials & Design*, vol. 233, p. 112 171, 2023. DOI: 10.1016/j.matdes.2023.112171.

[25] L. Odoni, "Propriétés mécaniques et effets d'échelle," Ecole centrale de Lyon, 1999.

[26] I. N. Sneddon, "The Relation between Load and Penetration in the Axisymmetric Boussinesq Problem for a Punch of Arbitrary Profile," *International Journal of Engineering Science*, vol. 3, pp. 47–57, 1965. DOI: 10.1016/0020-7225(65)90019-4.

[27] J. J. Vlassak and W. D. Nix, "Indentation modulus of elastically anisotropic half spaces," *Philosophical Magazine A*, vol. 67, no. 5, pp. 1045–1056, 1993. DOI: 10.1080/01418619308224756.

[28] J. J. Vlassak and W. Nix, "Measuring the elastic properties of anisotropic materials by means of indentation experiments," *Journal of the Mechanics and Physics of Solids*, vol. 42, no. 8, pp. 1223–1245, 1994. DOI: 10.1016/0022-5096(94)90033-7.

[29] J. J. Vlassak, M. Ciavarella, J. R. Barber, and X. Wang, "The indentation modulus of elastically anisotropic materials for indenters of arbitrary shape," *Journal of the Mechanics and Physics of Solids*, vol. 51, no. 9, pp. 1701–1721, 2003. DOI: 10.1016/S0022-5096(03)00066-8.

[30] T. S. Guruprasad, V. Keryvin, L. Charleux, J. .-. Guin, and O. Arnould, "On the determination of the elastic constants of carbon fibres by nanoindentation tests," *Carbon*, vol. 173, pp. 572–586, 2021. DOI: 10.1016/j.carbon.2020.09.052.

[31] G. Kermouche, J. Loubet, and J. Bergheau, "Extraction of stress–strain curves of elastic–viscoplastic solids using conical/pyramidal indentation testing with application to polymers," *Mechanics of Materials*, vol. 40, no. 4-5, pp. 271–283, 2008. DOI: 10.1016/j.mechmat.2007.08.003.

[32] M. F. Doerner and W. D. Nix, "A method for interpreting the data from depth-sensing indentation instruments," *Journal of Materials Research*, vol. 1, no. 4, pp. 601–609, 1986. DOI: 10.1557/JMR.1986.0601.

[33] M. Mayo and W. Nix, "A micro-indentation study of superplasticity in Pb, Sn, and Sn-38 wt% Pb," *Acta Metallurgica*, vol. 36, no. 8, pp. 2183–2192, 1988. DOI: 10.1016/0001-6160(88)90319-7.

[34] M. Lodes, A. Hartmaier, M. Göken, and K. Durst, "Influence of dislocation density on the pop-in behavior and indentation size effect in CaF_2 single crystals: Experiments and molecular dynamics simulations," *Acta Materialia*, vol. 59, no. 11, pp. 4264–4273, 2011. DOI: 10.1016/j.actamat.2011.03.050.

[35] A. Aruga, R. B. Inturi, J. A. Barnard, and R. C. Bradt, "Mechanical Properties of CaF_2 Single Crystal Substrates Determined from Nanoindentation Techniques," *MRS Proceedings*, vol. 436, p. 213, 1996. DOI: 10.1557/PROC-436-213.

[36] V. Maier, C. Schunk, M. Göken, and K. Durst, "Microstructure-dependent deformation behaviour of bcc-metals – indentation size effect and strain rate sensitivity," *Philosophical Magazine*, vol. 95, no. 16-18, pp. 1766–1779, 2015. DOI: 10.1080/14786435.2014.982741.

[37] W. Hermann, H. Sockel, J. Han, and A. Bertram, "Elastic Properties and Determination of Elastic Constants of Nickel-Base Superalloys by a Free-Free Beam Technique," in *Superalloys 1996 (Eighth International Symposium)*, TMS, 1996, pp. 229–238. DOI: 10.7449/1996/Superalloys_1996_229_238.

[38] J. B. O'Neill, B. A. W. Redfern, and C. A. Brookes, "Anisotropy in the hardness and friction of calcium fluoride crystals," *Journal of Materials Science*, vol. 8, no. 1, pp. 47–58, 1973. DOI: 10.1007/BF00755582.

[39] S. R. Mekala, "Analysis of creep transients in calcium fluoride single crystals following stress changes," doctoralthesis, Friedrich-Alexander-Universität Erlangen-Nürnberg (FAU), 2006.

[40] H. Conrad, "Thermally activated deformation of metals," *JOM*, vol. 16, no. 7, pp. 582–588, 1964. DOI: 10.1007/BF03378292.

[41] D. Caillard and J.-L. Martin, *Thermally Activated Mechanisms in Crystal Plasticity* (Pergamon Materials Series 8). Amsterdam ; Boston, Mass: Pergamon, 2003, 433 pp.

[42] G. A. Keig and R. L. Coble, "Mobility of Edge Dislocations in Single-Crystal Calcium Fluoride," *Journal of Applied Physics*, vol. 39, no. 13, pp. 6090–6095, 1968. DOI: 10.1063/1.1656121.

[43] A. G. Evans and P. L. Pratt, "Dislocations in the fluorite structure," *Philosophical Magazine*, vol. 20, no. 168, pp. 1213–1237, 1969. DOI: 10.1080/14786436908228207.

[44] P. Jain, S. Kim, R. E. Youngman, and S. Sen, "Direct Observation of Defect Dynamics in Nanocrystalline CaF_2: Results from 19F MAS NMR Spectroscopy," *The Journal of Physical Chemistry Letters*, vol. 1, no. 7, pp. 1126–1129, 2010. DOI: 10.1021/jz100152j.

[45] W. L. Phillips, "Deformation and Fracture Processes in Calcium Fluoride Single Crystals," *Journal of the American Ceramic Society*, vol. 44, no. 10, pp. 499–506, 1961. DOI: 10.1111/j.1151-2916.1961.tb13713.x.

[46] K. Kishan Rao and D. B. Sirdeshmukh, "Indentation studies on alkaline earth fluoride crystals at elevated temperatures," *Pramāṇa*, vol. 34, pp. 151–156, 1990. DOI: 10.1007/BF02847199.

[47] A. Munoz, A. Dom, and J. Castaing, "Slip systems and plastic anisotropy in CaF_2," *Journal Of Materials Science*, vol. 29, pp. 6207–6211, 1994. DOI: 10.1007/BF00354561.

[48] W. Bontinck, "The hydrolysis of solid CaF_2," *Physica*, vol. 24, no. 6, pp. 650–658, 1958. DOI: 10.1016/S0031-8914(58)80079-8.

[49] W. L. Phillips Jr. and J. E. Hanlon, "Oxygen Penetration Into Single Crystals of Calcium Fluoride," *Journal of the American Ceramic Society*, vol. 46, no. 9, pp. 447–449, 1963. DOI: 10.1111/j.1151-2916.1963.tb11773.x.

[50] S. R. Sashital and K. Vedam, "Hardening of CaF_2 single-crystal surfaces due to contamination by atmospheric oxygen," *Journal of Applied Physics*, vol. 43, no. 11, pp. 4396–4400, 1972. DOI: 10.1063/1.1660933.

[51] K. Kubo, "Optical Studies on Electrolytically Colored CaF_2 Crystals," *Journal of the Physical Society of Japan*, vol. 21, no. 6, pp. 1046–1053, 1966.

[52] Hj. Matzke and R. Lindner, "Diffusion von Ca-45 in CaF_2," *Zeitschrift für Naturforschung A*, vol. 19, no. 10, pp. 1178–1180, 1964. DOI: 10.1515/zna-1964-1008.

[53] L. E. Jones, "High-temperature elasticity of the fluorite-structure compounds CaF_2, SrF_2 and BaF_2," *Physics of the Earth and Planetary Interiors*, vol. 15, no. 1, pp. 77–89, 1977. DOI: 10.1016/0031-9201(77)90012-7.

[54] F. Bachmann, R. Hielscher, and H. Schaeben, "Grain detection from 2d and 3d EBSD data—Specification of the MTEX algorithm," *Ultramicroscopy*, vol. 111, no. 12, pp. 1720–1733, 2011. DOI: 10.1016/j.ultramic.2011.08.002.

[55] P. Sudharshan Phani and W. Oliver, "A critical assessment of the effect of indentation spacing on the measurement of hardness and modulus using instrumented indentation testing," *Materials & Design*, vol. 164, p. 107 563, 2019. DOI: 10.1016/j.matdes.2018.107563.

[56] C. Su, E. G. Herbert, S. Sohn, J. A. LaManna, W. C. Oliver, and G. M. Pharr, "Measurement of power-law creep parameters by instrumented indentation methods," *Journal of the Mechanics and Physics of Solids*, vol. 61, no. 2, pp. 517–536, 2013. DOI: 10.1016/j.jmps.2012.09.009.

[57] G. Guillonneau *et al.*, "Nanomechanical testing at high strain rates: New instrumentation for nanoindentation and microcompression," *Materials & Design*, vol. 148, pp. 39–48, 2018. DOI: 10.1016/j.matdes.2018.03.050.